arXiv:1410.1792v1 [physics.atom-ph] 7 Oct 2014

Angular distributions in two-colour two-photon ionization of He

H.F. Rey[1,*] and H.W. van der Hart[1]

[1] *Centre for Theoretical Atomic, Molecular and Optical Physics, School of Mathematics and Physics Queen's University Belfast, Belfast BT7 1NN, United Kingdom*

(Dated: October 8, 2014)

We present R-Matrix with time dependence (RMT) calculations for the photoionization of helium irradiated by an EUV laser pulse and an overlapping IR pulse with an emphasis on the anisotropy parameters of the sidebands generated by the dressing laser field. We investigate how these parameters depend on the amount of atomic structure included in the theoretical model for two-photon ionization. To verify the accuracy of the RMT approach, our theoretical results are compared with experiment.

PACS numbers: 31.15.A-,32.80.Rm

I. INTRODUCTION

Over the last 15 years significant progress has been made in the development of light sources, capable of generating ultra-short pulses lasting just a fraction of a femtosecond [1]. One of the key experimental challenges has been the characterisation of these light pulses [2]. By overlapping the ultra-short pulse with an IR pulse during an ionization process, sidebands are observed in photoelectron spectra. Examination of these sidebands allows the extraction of the phase differences between the different harmonic constituents of the ultra-short pulse [3]. Knowledge of these phase differences then allows the reconstruction of the ultra-short light pulse.

Interest in sidebands created when photoionization by high-frequency light occurs in the presence of an IR field is not just limited to the characterisation of ultra-short light pulses. With the advent of free-electron lasers operating at high photon energies [4–6], the interplay between EUV photons and IR photons in the photoionization process [7] can give valuable information about the time delay between the EUV and the IR pulse.

The experimental interest in sidebands generated by the addition of an IR field to an EUV field should be complemented by theoretical investigation. A good description of these sidebands is given by the soft-photon approximation (SPA) [8], in which the angular distribution of the ejected electron is modified by Bessel functions, depending on the number of IR photons absorbed and the angle at which the electron is emitted with respect to the polarization direction. This approximation applies when the energy of the IR photon is much larger than the energy of electrons emitted by the EUV field by itself. When the energies of the emitted electron and the IR photon are comparable, the ionic potential will affect the motion of the outgoing electron, and the predictions of the SPA may not be as accurate.

In the present study, we investigate the effect of the residual ionic potential on the angular distributions of sidebands generated during EUV+IR photoionization of He using the R-matrix including time-dependence (RMT) approach [9–11]. The He atom has been chosen, since the angular distributions of the photoelectron ejected in two-colour fields have been the subject of experimental investigation, either when the EUV pulse is sufficiently energetic to eject an electron from He [12, 13], or when the pulse excites one of the 1s electrons to an excite np state [14, 15]. In addition, for He, it is straightforward to change the amount of atomic structure retained in the calculations. A similar study of photo-electron angular distributions has recently been performed for Ar using the time-dependent R-matrix (TDRM) approach [16], including a comparison with experiment [17], the SPA [8] and model potential anisotropy parameters [18]. The present calculation thus also allows us to assess the computational efficiency of the two different time-dependent R-matrix approaches.

The RMT approach was developed only a few years ago[9–11], and has since been applied to study time delays in photoionization of Ne [19], to two-photon double ionization of He [20], and to IR-assisted photoionization of Ne^+ [21]. Similar to the TDRM approach [22], it employs the standard R-matrix technique of separating configuration space into an inner region and an outer region. However, the wavefunction is propagated using an Arnoldi approach [23, 24] in the RMT approach, compared to a Crank-Nicholson scheme in the TDRM approach. Spatially, the TDRM approach applies a sequential R-matrix propagation scheme, which restricts the degree of parallelisation to about 100-200 processors. This sequential step does not occur within the RMT approach, and it can therefore be efficiently parallelised over substantially larger numbers of processors [20].

In the present report, we will first describe the RMT approach and indicate the differences between the RMT approach and the TDRM approach. We then apply the RMT approach to two-colour two-photon ionization of He, and present the associated anisotropy parameters. We briefly investigate how these parameters depend on the theoretical description of He. We compare the obtained parameters to those obtained experimentally as

*Electronic address: h.rey@qub.ac.uk

well as the predictions from the SPA.

II. THE R-MATRIX INCLUDING TIME APPROACH

The R-matrix including time (RMT) approach is a new *ab initio* method to solve accurately the time dependent Schrödinger equation (TDSE) for multi-electron atoms in intense laser light [9–11]. The approach adopts the standard R-matrix approach [25] of splitting configuration space into two distinct regions: an inner region and an outer region. In the inner region, all $N+1$ electrons in the system are contained within a sphere of radius b around the nucleus of the atom. N therefore indicates the number of electrons left on the ion after a single electron has been ejected. In the outer region N electrons still remain within the sphere of radius b, but one of the electrons has now left the sphere, so that its radial distance from the nucleus, r_{N+1}, is larger than b.

In the inner region, a standard R-matrix basis expansion is used to describe the wave function [25]. In this expansion, states of the system under investigation are described in terms of antisymmetrised direct products of residual-ion states with a full continuum basis for the outgoing electron. Additional correlation orbitals can be included to improve the description of the system. All interactions are accounted for in the Hamiltonian, including electron exchange and correlation effects between all pairs of electrons.

In the outer region, the wavefunction is described in terms of a direct product of residual-ion states, coupled with the spin and angular momentum of the outgoing electron, with the radial wavefunction for the outgoing electron. Since the outer electron is separated from the other electrons, its wavefunction can be treated separately from the others, and hence exchange effects can be neglected. In the RMT method, the radial wavefunction for the outer electron is described in terms of a finite difference grid, similar to the approach pursued in the HELIUM codes [23]. This is the first difference compared to the TDRM approach [22], in which the wave function was described in terms of a very dense set of B-spline functions.

In sections II A and II B, we give a brief overview of the theory underpinning the RMT approach. A full description of the approach is given in [10, 11]. To obtain the properties of the system under investigation, we start with the time-dependent Schrödinger equation (TDSE),

$$i\frac{\partial}{\partial t}\Psi(\mathbf{X}_{N+1},t) = H_{N+1}(t)\Psi(\mathbf{X}_{N+1},t), \tag{1}$$

where H_{N+1} is the full Hamiltonian for the system, given by:

$$H_{N+1} = \sum_{i=1}^{N+1}\left(-\frac{1}{2}\bigtriangledown_i^2 - \frac{Z}{r_i} + \sum_{i>j=1}^{N+1}\frac{1}{r_{ij}} + \mathbf{E}(t)\cdot\sum_{i=1}^{N+1}\mathbf{r_i}\right). \tag{2}$$

In this equation $\mathbf{X}_{N+1} \equiv \boldsymbol{x}_1, \boldsymbol{x}_2, \ldots, \boldsymbol{x}_{N+1}$ and $\boldsymbol{x}_i \equiv \boldsymbol{r}_i\sigma_i$, with $\boldsymbol{r}_i$ and $\boldsymbol{\sigma}_i$ the position and spin vectors of the i^{th} electron, respectively. Z indicates the nuclear charge and $\boldsymbol{E}(t)$ is the electric field of the light pulse. Furthermore, $r_{ij} = |\boldsymbol{r}_i - \boldsymbol{r}_j|$. The nucleus has been taken at the origin of the coordinate system.

A. The outer region

In the outer region the $(N+1)$-electron wavefunction is expanded as follows [25]:

$$\Psi(\mathbf{X}_{N+1},t) = \sum_p \overline{\Phi}_p(\mathbf{X}_N;\hat{\boldsymbol{r}},\sigma_{N+1})\frac{1}{r}F_p(r,t), \tag{3}$$

where $r \equiv r_{N+1}$ is the radial distance of the $(N+1)^{\text{th}}$ electron. The channel functions $\overline{\Phi}_p$ are formed by coupling relevant states of the residual N-electron ionic system $\Phi_T(X_N)$ with angular and spin components of the ejected-electron wavefunction. The functions $F_p(r,t)$ describe the radial wavefunction of the outer electron in the p^{th} channel.

By left-projecting the TDSE (1) onto the channel functions $\overline{\Phi}_p$, and integrating over all spatial and spin coordinates except r, equation (1) can be rewritten in terms of a set of coupled partial differential equations for $F_p(r,t)$ [10, 11]:

$$\begin{aligned} i\frac{\partial}{\partial t}F_p(r,t) &= h_{II_p}(r)F_p(r,t) + \sum_{p'}[W_{E_{pp'}}(r) + W_{D_{pp'}}(t) \\ &+ W_{P_{pp'}}(r,t)]F_{p'}(r,t), \end{aligned} \tag{4}$$

where $h_{II_p}(r)$ describes the energy of the residual-ion state, the kinetic energy, the screened nuclear attraction and centrifugal repulsion for the outer electron,

$$h_{II_p}(r) = -\frac{1}{2}\frac{d^2}{dr^2} + \frac{l_p(l_p+1)}{2r^2} - \frac{Z-N}{r} + E_p. \tag{5}$$

The other terms in equation (4) describe the coupling between the different channels. $W_{E_{pp'}}(r)$ describes the coupling due to long-range repulsion terms arising from the residual electrons, excluding the screening term,

$$W_{E_{pp'}}(r) = \left\langle r^{-1}\overline{\Phi}_p \left| \sum_{j=1}^{N}\frac{1}{|\mathbf{r}-\mathbf{r_j}|} - \frac{N}{r}\right| r^{-1}\overline{\Phi}_{p'}\right\rangle. \tag{6}$$

$W_{D_{pp'}}(t)$ describes the coupling due to interaction between the light field and the residual-ion states,

$$W_{D_{pp'}}(t) = \left\langle r^{-1}\overline{\Phi}_p \left| \mathbf{E}(t)\cdot\sum_{i=1}^{N}\boldsymbol{r_i}\right| r^{-1}\overline{\Phi}_{p'}\right\rangle. \tag{7}$$

Finally, $W_{P_{pp'}}(t)$ describes the coupling due to interaction between the light field and the outer electron,

$$W_{P_{pp'}}(r,t) = \left\langle r^{-1}\overline{\Phi}_p \left|\mathbf{E}(t)\cdot\boldsymbol{r}\right| r^{-1}\overline{\Phi}_{p'}\right\rangle. \tag{8}$$

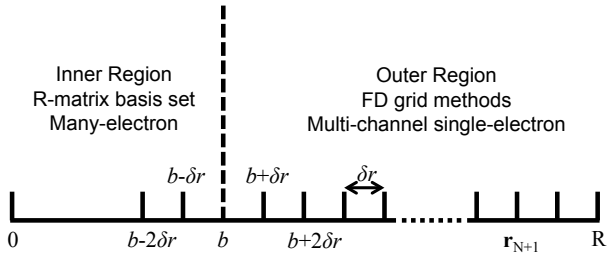

FIG. 1: The R-matrix division-of-space concept. In the inner region a basis expansion of the wavefunction is chosen, while in the outer region a grid-based representation is considered. The vertical dashes indicate the grid points used in the calculation. The outer-region grid extrapolates into the inner region. At these points, the inner region wavefunction is projected onto the outer-region grid associated with each channel. The boundary of the inner region is at $r = b$ and the outer region boundary is at $r = R$.

Equation (4) describes a system of equations, which can be solved efficiently using finite-difference techniques [10, 11]. The radial wavefunction for the outer electron, $F_p(r,t)$, is discretised on a radial grid as shown in figure 1. The potential-energy terms and the angular-momentum repulsion term can be determined directly at each grid point for each channel. The second derivative term in the kinetic energy operator is implemented using a five-point finite-difference rule. Near the boundary with the inner region, wavefunction information from the inner region is required. We therefore extend the finite difference grid into the inner region by $2N_A$ points, where N_A is the order of the Arnoldi propagator. Following the determination of the inner-region field-free eigenstates, we project these inner-region eigenstates onto the channel functions. Using the time-dependent coefficients $C_k(t)$ associated with the field-free inner-region eigenstates (see section II B), we can evaluate the time-dependent inner-region wavefunction on the finite-difference grid extension into the inner region (eg. the points $b-\delta r$ and $b-2\delta r$ in figure 1). Once the wavefunction is known on these points, all required orders of the kinetic energy operator can be evaluated accurately in the outer region. To propagate the outer region wavefunction in time from t to $t+\delta t$ we employ the Arnoldi propagator [23, 24].

The most demanding part in the solution of equation (4) in the present approach is the evaluation of the right-hand side. This is effectively a matrix-vector multiplication, where the matrix will be sparse due to the angular-momentum constraints on the individual matrix elements. On the other hand, solution of the outer-region equations in the TDRM approach requires the (computationally demanding) determination of time-dependent Green's functions across the entire outer region [22]. In addition, the TDRM approach determines the updated wavefunction through an R-matrix propagation scheme, which cannot be carried out in parallel. In the RMT approach, the updated wavefunction is obtained through a purely local computational scheme, and can therefore be parallelised over very large numbers of cores. As a consequence, the RMT codes are substantially faster than the TDRM codes, especially for large-scale problems.

B. The inner region

The time dependent $(N+1)$-electron wavefunction in the inner region $\Psi_I(X_{N+1},t)$ is expanded over field-free eigenstates of the Hamiltonian in the inner region $\psi_k(X_{N+1})$ as follows [25]:

$$\Psi_I(X_{N+1},t) = \sum_k C_k(t)\psi_k(X_{N+1}), \tag{9}$$

where all $r_i \leq b$ and the $C_k(t)$ are the time-dependent expansion coefficients associated with the field-free eigenstates.

The TDSE in the inner region is given by:

$$i\frac{\partial}{\partial t}\Psi(X_{N+1},t) = H_{N+1}(t)\Psi(X_{N+1},t), \tag{10}$$

where the time-dependent Hamiltonian is the same as given in expression (2). However, in the inner region, the Hamiltonian $H_{N+1}(t)$ cannot be hermitian. Ionization requires an electron to escape to infinity, and for this to occur, some part of the wavefunction must have left the inner region. Hence the total population in the inner region cannot be conserved. The non-hermiticity arises in the evaluation of the kinetic energy operator at the boundary. In the determination of the field-free inner-region eigenstates, however, this non-hermiticity is compensated for through the addition of a Bloch operator [25],

$$\mathcal{L}_{N+1} = \frac{1}{2}\sum_{i=1}^{N+1}\delta(r_i-b)\left(\frac{d}{dr_i} - \frac{g_0-1}{r_i}\right), \tag{11}$$

where the value of g_0 can, in principle, be chosen freely.

To propagate the inner-region wavefunction in time using the correct time-dependent Hamiltonian, we therefore have to remove the Bloch operator [10, 11]:

$$i\frac{\partial}{\partial t}\Psi_I(X_{N+1},t) = H_I(t)\Psi_I(X_{N+1},t) - \mathcal{L}_{N+1}\Psi_I(X_{N+1},t), \tag{12}$$

where H_I is the inner-region Hamiltonian including the Bloch operator. However, since the Bloch operator only acts on the wavefunction at the boundary, we can apply the Bloch operator upon the outer-region wavefunction instead of the inner-region wavefunction:

$$i\frac{\partial}{\partial t}\Psi_I(X_{N+1},t) = H_I(t)\Psi_I(X_{N+1},t) - \mathcal{L}_{N+1}\Psi(X_{N+1},t). \tag{13}$$

We now expand the inner-region wavefunction in terms of the field-free eigenstates $\psi_k(X_{N+1})$, and project the inner region TDSE (12) onto these eigenstates. This projection

then provides a set of equations for the time evolution of the coefficients $C_k(t)$:

$$\frac{d}{dt}C_k(t) = -i\sum_{k'} H_{I_{kk'}}(t)C_{k'}(t) + \frac{i}{2}\sum_p \omega_{pk}\frac{\partial F_p(r,t)}{\partial r}\bigg|_{r=b}, \tag{14}$$

where $H_{I_{kk'}}(t)$ is the time-dependent Hamiltonian matrix element between field-free states ψ_k and $\psi_{k'}$, and ω_{pk} are the surface amplitudes of eigenstate ψ_k with respect to outer region channel p [25].

Using the approximation that the time-dependent Hamiltonian is constant within the time interval $[t, t+\delta t]$, we can now obtain an approximate solution to the inner-region TDSE (10) in terms of the so-called ϕ functions [26]. In matrix notation [10, 11, 27],

$$\mathbf{C}(t+\delta t) \approx e^{-i\delta t\mathbf{H}_I}\mathbf{C}(t) + \sum_{j=1}^{n_j}(\delta t)^j\,\phi_j(-i\delta t\mathbf{H}_I)\mathbf{U}_j(t), \tag{15}$$

where

$$\mathbf{U}_0(t) = \mathbf{C}(t), \qquad \boldsymbol{U}_j(t) = i\frac{d^{j-1}}{dt^{j-1}}\boldsymbol{S}(t), \tag{16}$$

with

$$\mathbf{S}(t) = \frac{1}{2}\sum_p \omega_{pk}\frac{\partial F_p(r,t)}{\partial r}\bigg|_{r=b}. \tag{17}$$

The ϕ_j functions can be regarded as "shifted" exponentiation functions, as can be appreciated through their Taylor series [11],

$$\phi_j(z) = \sum_{k=0}^{\infty}\frac{z^k}{(k+j)!}. \tag{18}$$

For the propagation of the inner region wavefunction, we again use an Arnoldi method [23, 24]. However, we now need separate propagators to evaluate each of the ϕ-functions as well as the $\exp(-i\delta t\mathbf{H}_I)$ term. Thus each of the $\mathbf{U}_j$ terms in equation (15) is propagated separately, and the final wavefunction at time $t+\delta t$ is obtained by combining all terms.

C. Description of He and field parameters

Our interest focuses on the anisotropy parameters in two-colour photoionization of He and the amount of atomic structure included in the theoretical description. Hence we describe the He atom using three different basis expansions. These basis expansions can be characterised by the residual He^+-ion states retained in the calculations. The He basis is built by combining these residual ion states with a complete set of continuum and bound-state functions for a single outgoing electron. The simplest basis expansion included employs only the 1s state of He^+ as a residual-ion state. Hence the He basis contains all $1sn/\varepsilon\ell$ states. The second basis set we employed including the 1s, 2s and 2p states of He^+ as residual-ion states, so that the He basis contains all $1sn/\varepsilon\ell$, $2sn/\varepsilon\ell$ and $2pn/\varepsilon\ell$ states. For the third basis set, we use pseudo-orbitals, $\overline{2s}$ and $\overline{2p}$, as residual-ion states rather than the physical 2s and 2p orbitals. These pseudo-orbitals are constructed as Sturmian-type orbitals $r^i e^{-\alpha r}$ with the same exponential decay as the 1s orbital, minimal power of the polynomial term, and orthogonality with respect to the 1s orbital. These basis sets are similar to the ones employed in the investigation of the choice of gauge for the laser field for time-dependent R-matrix theory [28].

RMT calculations require a choice for the maximum angular momentum to be included within the calculations. The calculations using the 1s residual-ion state only were performed with 3 different values for the maximum angular momentum, $L_{\max} = 5$, $L_{\max} = 7$, and $L_{\max} = 9$, with the last two calculations producing very similar results. We therefore report results for all three basis sets investigated using a maximum angular momentum $L_{\max} = 7$.

In the generation of the He basis, we have used an R-matrix inner region radius of 20 a_0. This inner region is sufficiently large to contain the He ground state. The basis used for the description of the continuum electron within the inner electron contains 70 B-splines with order $k = 11$. The knot point distribution varies from a nearly quadratic spacing near the nucleus to a nearly linear spacing near the inner region boundary. Additional knot points are inserted further inward to improve the description of functions close to the nucleus. The outer region radial wavefunction for the ejected electron is described on a finite difference grid extending to 1200 a.u. with a grid spacing $\delta r = 0.075$ a_0. The time step in the propagation is set to $\delta t = 0.005$ a.u. The order of the Arnoldi propagator is 14.

We investigate ionization of helium irradiated by a combination of two laser pulses: an EUV pulse corresponding to the $17^{\text{th}} - 21^{\text{st}}$ harmonic of the fundamental laser field and an overlapping fundamental dressing field. The wavelength of the fundamental field ranges from $790 - 810$ nm and were chosen closely to resemble those used in the experiment [13]. The IR laser field considered is linearly polarized in the z-direction with an intensity of 5×10^{10} W cm^{-2} at peak. The IR pulse profile is given by a 3-cycle $\sin^2$ ramp on, followed by 2 cycles at a peak intensity and a 3-cycle $\sin^2$ ramp off (3-2-3). The EUV laser field considered is linearly polarized in the z-direction with a peak intensity of 1×10^{11} W cm^{-2}. The EUV pulse profile is given by a $3n$-cycle $\sin^2$ ramp on, followed by $2n$ cycles at a peak intensity and a $3n$-cycle $\sin^2$ ramp off (3-2-3), where n indicates the order of the EUV harmonic. Following the end of the pulse, the wavefunction is propagated in time corresponding to just over 2.8 cycles of the IR field to ensure that the outgoing electron is well separated from the residual ion and to ensure that the ejected electron is indeed a continuum

electron.

III. RESULTS

In this report, we investigate the asymmetry parameters of two-colour two-photon ionization of He irradiated by a combination of a short EUV pulse and a short IR pulse using the RMT approach. These parameters can be obtained from the final-time wavefunction obtained at the end of the calculations. This wavefunction is described in terms of total angular momentum, whereas the experimental observations relate primarily to the ejected electron. In order to compare the results from our investigations to experiment, we therefore first have to decouple the wavefunction of the outer electron and the wavefunction of the residual ion states using Clebsch-Gordan coefficients [29]. Following this decoupling, we can construct the spatial wavefunction for the outgoing electron. This spatial wavefunction is then transformed into a momentum distribution for the outgoing electron under the assumption that the Coulomb potential of the residual ion can be neglected.

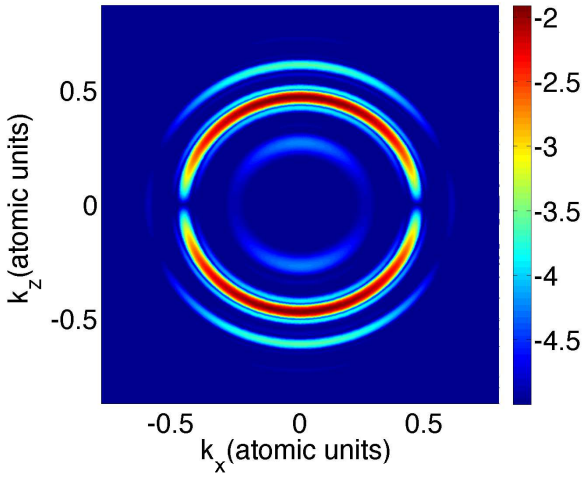

FIG. 2: (Colour online) Photoelectron momentum spectrum in the $k_x k_z$ plane for helium irradiated by an IR field with wavelength of 790 nm and its 17$^{\text{th}}$ harmonic.

Figure 2 shows the ejected-electron momentum distribution of the ejected electron in the $k_x k_z$-plane for the case that He is irradiated by an IR laser field with a wavelength of 790 nm and an EUV field given by the 17$^{\text{th}}$ harmonic of the IR field. The IR field is relatively weak, and we therefore show the momentum distribution on a logarithmic scale. The photoionization spectrum is dominated by the central EUV photoionization peak at $|k| \approx 0.45$ atomic units. Since the central peak is given by a p outgoing electron, a node is clearly visible at $k_z = 0$ for this central peak. The sidebands generated by absorption or emission of an additional IR photon can also be identified easily in figure 2. As will be illustrated later in more detail, these sidebands show no node at $k_z = 0$.

The relative magnitudes between the central EUV peak and the sidebands can be better assessed in figure 3, which shows the photoelectron momentum spectra along the laser polarization axis for a 790-nm IR field and its 17$^{\text{th}}$ harmonic. The figure shows that for the present laser parameters (short IR pulse, weak intensity), the photoelectron momentum spectrum is dominated by the central photoemission peak, whereas the sidebands are significantly weaker in intensity. Two sidebands can be seen immediately by the side of the main EUV photoelectron peak. These peaks originate from the pulse shape of the EUV laser pulse, which introduces additional frequency components. The sidebands associated with absorption or emission of an additional IR photon are well separated from the main EUV peak, and we can thus easily obtain a total intensity for each of the sidebands at a given emission angle by integration over the sideband.

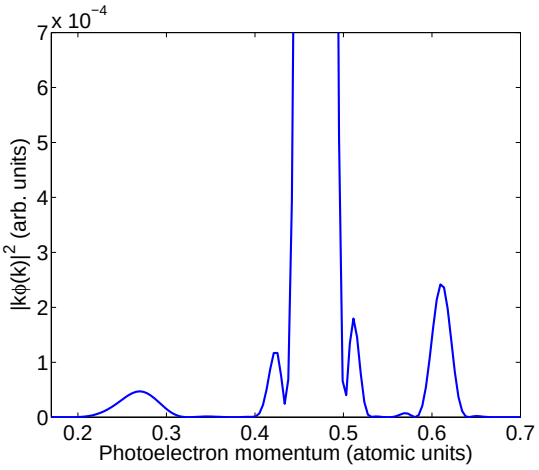

FIG. 3: (Colour online) Photoelectron momentum spectrum for helium irradiated by a 790-nm IR field and its 17$^{\text{th}}$ harmonic along the polarization axis of the two laser fields. The momentum spectrum shows that, for an eight-cycle IR-pulse with peak intensity of 5×10^{10} W/cm^2, the spectrum is dominated by the central EUV peak. Two further sidebands can be seen directly by the side of the EUV pulse. These originate from the EUV pulse shape.

The asymmetry parameters for the two-colour two-photon ionization process describe the variation of the sideband intensity with emission angle, relative to the laser polarization axis, θ. Figure 4 shows the variation of the integrated sideband intensity with $\cos\theta$ for the case of a 790-nm IR field and its 17$^{\text{th}}$ harmonic. The figure demonstrates that the positive sideband (absorption of an IR photon) and the negative sideband (emission of an IR photon) show significant differences. This difference between positive and negative sidebands, and hence differences in the asymmetry parameters, has already been observed before in studies of Ar [16, 17]. Figure 4 shows that the angular distribution for the higher sideband is more peaked along the laser polarization axis, whereas

the negative sideband shows a more constant behaviour as a function of angle.

This difference between positive and negative sideband is not too unexpected. The present choice of laser parameters means that the lower sideband corresponds to emission of electrons with an energy of only 0.8 eV, less than the IR photon energy. At this small energy, interactions with the residual ion can become important. Furthermore, the centrifugal repulsion potential can significantly affect the angular distribution. Whereas s electrons do not see this repulsive potential, d electrons do. The classical turning point for a d electron with an energy corresponding to the negative sideband is about 2.8 a_0, whereas it is about 1.8 a_0 at an energy corresponding to the positive sideband. Hence, the overlap between the d continuum and the He ground state will be significantly greater for the higher sideband than for the lower sideband. The emission in the lower sideband should then be more isotropic than the emission in the higher sideband.

Once we have obtained the angular distributions associated with the sidebands, we can use them to derive the anisotropy parameters. It is also possible to derive the anisotropy parameters using a perturbative approach, in which one can derive the anisotropy parameters from the magnitude and relative phase between the excitation of the s and the d continuum. In the present time-dependent calculation, we have chosen not to use the latter method, as g and $\ell = 6$ channels are also populated during the calculations. Since these channels can receive population, they should be included in the determination of the anisotropy parameters. We also include possible contributions from p, f and $\ell = 5$ and 7 channels, even though, for long weak pulses, they do not contribute to two-photon ionization.

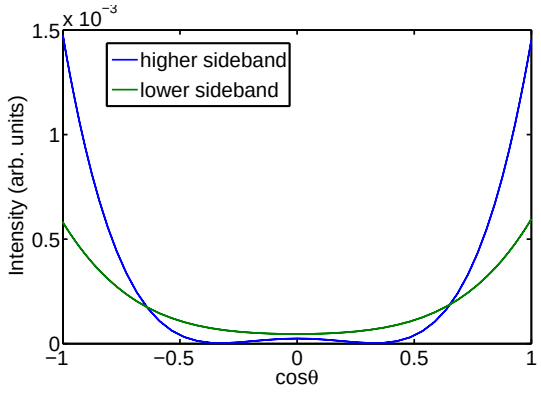

FIG. 4: (Colour online) Intensities of the negative (lower) and positive (higher) sidebands as a function of $\cos\theta$ for He irradiated by the 17$^{\text{th}}$ harmonic and overlapping fundamental of the 790 nm pulse.

The photoelectron angular distributions for two-photon ionization are given in terms of the anisotropy parameters by [17]

$$I(\theta) = \frac{\sigma}{4\pi}[1 + \beta_2 P_2(\cos\theta) + \beta_4 P_4(\cos\theta)], \qquad (19)$$

where θ is the angle between the laser polarization vector and electron velocity vector, σ is the total cross section, and β_2 and β_4 are the anisotropy parameters associated with the second and fourth order Legendre polynomials, respectively. We can thus obtain these parameters by fitting this formula to the theoretical angular distribution. For the data in figure 4, this gives anisotropy parameters of $\beta_2 = 1.83$ and $\beta_4 = 0.48$ for the negative sideband, and $\beta_2 = 3.03$ and $\beta_4 = 1.62$ for the positive sideband.

In the recent experimental investigation of the anisotropy parameters [13], six combinations of IR wavelength and associated harmonic were investigated. For an IR wavelength of 790 nm, and an EUV pulse given by its 17$^{\text{th}}$ harmonic, anisotropy parameters of $\beta_2 = 1.73 \pm 0.07$ and $\beta_4 = 0.55 \pm 0.19$ were obtained for the negative sideband, and anisotropy parameters of $\beta_2 = 2.96 \pm 0.08$ and $\beta_4 = 1.50 \pm 0.03$ were obtained for the positive sideband. Although the theoretical calculations lie slightly outside the experimental error bars for β_2 for the negative sideband and β_4 for the positive sideband, the overall agreement for this choice of laser wavelengths is very good. A more detailed comparison of the theoretical and experimental anisotropy parameters is given in table I, where anisotropy parameters are presented for all combinations reported experimentally.

For the case discussed above, an IR wavelength of 790 nm, and an EUV pulse given by its 17$^{\text{th}}$ harmonic, we also show in table I, a comparison of the anisotropy parameters obtained using the different He basis sets. The table shows that the differences in the anisotropy parameters with respect to basis size are minimal in the present calculations, with a change of 0.01 in β_2 for the negative sideband. This level of change is typical: the largest difference is seen for case A, where β_2 for the negative sideband increases to 1.45 when only the 1s state of He^+ is included. The changes between the different basis sets lie thus within the experimental uncertainty. We have therefore chosen to present results only for the case where the He basis is constructed using the He^+ 1s, $\overline{2s}$ and $\overline{2p}$ residual-ion states.

The anisotropy parameters calculated using the RMT method, shown in table I, are noticeably smaller in magnitude for the negative sideband than for the positive sideband. $\beta_2^{(+)}$ is very similar in all cases studied, with a value very close to 3. $\beta_2^{(-)}$ shows greater variation: it increases with increasing photon energy of the harmonic. The negative sideband straddles the ionization threshold at a wavelength of 810 nm. Just above the ionization threshold, ionization will be dominated by s electrons, and therefore the closer the negative sideband gets to the ionization threshold, the emission process should become more and more isotropic. However, it may be difficult to obtain accurate anisotropy parameters very close to threshold in the present calculations, as the wavefunction may need to be propagated for long times to separate population in high Rydberg states from population in the low-energy continuum. The β_4 parameters show variation in both cases: we find a relatively small de-

TABLE I: Experimental [13] and theoretical anisotropy parameters for sidebands generated by the 17^{th} to the 21^{st} harmonics of the IR pulse overlapped by the fundamental pulse in helium. Anisotropy parameters for the lower sidebands are denoted by the superscript $(-)$ whereas positive sidebands are denoted by $(+)$.

Case	Wavelenghts	$\beta_2^{(-)}$	$\beta_4^{(-)}$	$\beta_2^{(+)}$	$\beta_4^{(+)}$
A	810 nm 17^{th} HH experiment	2.00±0.14	0.45±0.11	2.70±0.14	1.12±0.06
	810 nm 17^{th} HH RMT (3 states with pseudo-orbitals)	1.42	0.41	3.02	1.66
B	801 nm 17^{th} HH experiment	1.04±0.09	0.30±0.06	2.98±0.08	1.54±0.06
	801 nm 17^{th} HH RMT (3 states with pseudo-orbitals)	1.65	0.45	3.02	1.64
C	794 nm 17^{th} HH experiment	1.52±0.10	0.20±0.07	2.83±0.08	1.38±0.13
	794 nm 17^{th} HH RMT (3 states with pseudo-orbitals)	1.77	0.47	3.03	1.62
D	790 nm 17^{th} HH experiment	1.73±0.07	0.55±0.19	2.96±0.08	1.50±0.03
	790 nm 17^{th} HH RMT (1 state)	1.83	0.48	3.03	1.62
	790 nm 17^{th} HH RMT (3 states with real orbitals)	1.84	0.49	3.03	1.62
	790 nm 17^{th} HH RMT (3 states with pseudo-orbitals)	1.84	0.49	3.03	1.62
E	810 nm 19^{th} HH experiment	2.07±0.05	0.30±0.09	2.87±0.06	0.80±0.03
	810 nm 19^{th} HH RMT (3 states with pseudo-orbitals)	2.32	0.67	3.03	1.49
F	790 nm 21^{st} HH experiment	2.06±0.05	0.13±0.08	2.43±0.06	0.46±0.06
	790 nm 21^{st} HH RMT (3 states with pseudo-orbitals)	2.55	0.82	2.99	1.38

crease in $\beta_4^{(+)}$ with increasing EUV energy, whereas the $\beta_4^{(-)}$ shows a steady increase.

We can compare our anisotropy parameters with predictions using the Soft Photon Approximation (SPA) [8]. In this approximation, it is assumed that the absorption of the IR photon does not significantly affect the energy of the outgoing electron. This approximation may not work well for the 17^{th} harmonic due to its proximity to the ionization threshold, but the approximation should be more appropriate for higher harmonics. If it is assumed that the IR intensity is weak, then simple analytic expressions can be derived for the anisotropy parameters, in terms of the single-photon anisotropy parameter, estimated at the energy of the sideband [13]:

$$\beta_2^{\pm} = \frac{5}{7}\left(\frac{14+11\beta_2^{(0)}}{5+2\beta_2^{(0)}}\right), \beta_4^{\pm} = \frac{36}{7}\left(\frac{\beta_2^{(0)}}{5+2\beta_2^{(0)}}\right). \quad (20)$$

For single-photon ionization of the He ground-state to just above the He^+ 1s threshold, only p electrons can be ejected, and therefore the parameter $\beta_2^{(0)} = 2$ at all photon energies considered here. Substitution of this value into the SPA estimates for the anisotropy parameters gives the following values, $\beta_2^{\pm} = 20/7 \approx 2.86$ and $\beta_4^{\pm} = 8/7 \approx 1.14$. The values shown in table I show that with increasing EUV-photon energy the anisotropy parameters change towards the SPA predictions, but that higher EUV-photon energies than studied here need to be considered for the SPA to provide close agreement.

Table I also provides a comparison of the experimentally obtained anisotropy parameters with the present ones. The agreement between theory and experiment is best for the case studied earlier: an IR field of 790 nm and the 17^{th} harmonic, case D in table I. For the other cases, significant differences are seen between the experimental results and the present theoretical results. The best agreement is seen for $\beta_2^{(+)}$, but for $\beta_2^{(-)}$, other than case D, the smallest difference is 0.25. For the β_4 parameters, reasonably good agreement is obtained for all cases involving the 17^{th} harmonic, but the differences become pronounced for the cases involving the 19^{th} and 21^{st} harmonic.

The origin of the differences between the experimental results and theory is unclear. The β_4 parameters can be related directly to the relative magnitude between the emission of a d electron and emission of an s electron [13]. The present results, in particular those for the negative sideband, are consistent with a picture in which the emission of d electron is reduced when one approaches the ionization threshold. Extrapolation of the numerical results to higher photon energy gives anisotropy parameters consistent with the predictions of the SPA. On the other hand, the present calculations use very clean laser pulses for both the IR and the EUV pulse. It is unrealistic to expect such a clean pulse for the EUV pulse experimentally, as it is obtained through harmonic generation. These differences in laser parameters may well be the root origin for the differences seen between theory and experiment.

IV. CONCLUSIONS

We have demonstrated the application of the RMT approach to the investigation of photoelectron angular distributions and anisotropy parameters derived from these angular distributions. The negative sidebands tend to be more isotropic than the positive sidebands. The obtained anisotropy parameters differ noticeably from the predictions of the SPA due to the proximity of the EUV photon energy to the ionization threshold. For increasing EUV photon energy, the anisotropy parameters move closer to the predictions of the SPA. The agreement with experiment is good for the case of an IR pulse with a

wavelength of 790 nm and an EUV pulse given by its 17^{th} harmonic, but notable differences are seen for other combinations of laser pulse.

The RMT approach has been developed recently for the investigation of atomic processes in intense ultrashort light fields. The present calculations demonstrate that the approach can be used to obtain photoelectron distributions. In the present study, we compare these distributions for the case that the IR field is weak, but the approach should also be capable of treating more intense IR fields. In these cases, the sideband structure becomes significantly more complicated [7], and it would be interesting to see how the approach compares to, for example, the SPA when more IR photons are absorbed by the ejected electron. Whereas calculations at low IR intensity can be carried out using either the TDRM or RMT approach, at high IR intensities, the RMT approach would be strongly preferred, as the RMT approach is more suitable for large-scale parallelisation. This increase in parallelisation scale becomes particularly important when many angular momenta need to be included in the calculations.

Acknowledgements

This research has been supported by the European Commission Marie Curie Initial Training Network CORINF and by the UK Engineering and Physical Sciences Research Council under grant no. EP/G055416/1. The authors would like to thank J.S. Parker and K.T. Taylor for assistance with the RMT codes and valuable discussions. The main development of the RMT codes was carried out by M.A. Lysaght and L.R. Moore. This work made use of the facilities of HECToR, the UK's national high-performance computing service, which was provided by UoE HPCx Ltd at the University of Edinburgh, Cray Inc and NAG Ltd, and funded by the Office of Science and Technology through EPSRC's High End Computing Programme.

[1] M. Ivanov and F. Krausz, *Rev. Mod. Phys.* **81**, 1634 (2009).
[2] P.M. Paul, E.S. Toma, P. Breger, G. Mullot, F. Augé, P. Balcou, H.G. Muller and P. Agostini, 2001 *Science* **292** 1689 (2001)
[3] V. Veniard, R. Taïeb and A. Maquet, *Phys. Rev. A* **54**, 721 (1996)
[4] M. Yabashi *et al*, *J. Phys. B* **46**, 164001 (2013)
[5] J. Feldhaus *et al*, *J. Phys. B* **46**, 164002 (2013)
[6] C. Bostedt *et al*, *J. Phys.B* **46**, 164003 (2013).
[7] S. Düsterer, L. Rading, P. Johnsson, A. Rouzee, A. Hundertmark, M.J.J. Vrakking, P. Radcliffe, M. Meyer, A.K. Kazansky and N.M. Kabachnik, *J. Phys. B* **46**, 164026 (2013)
[8] A. Maquet and R. Taïeb, *J. Mod. Opt.* **54**, 1847 (2007).
[9] L.A.A. Nikolopoulos, J.S. Parker and K.T. Taylor, *Phys. Rev. A* **78**, 063420 (2008).
[10] L. R. Moore, M.A. Lysaght, L.A.A. Nikolopoulos, J.S. Parker, H.W. van der Hart and K.T. Taylor, *J. Mod. Opt.* **58**, 1132 (2011).
[11] M. A. Lysaght, L. R. Moore, L. A. A. Nikolopoulos, J. S. Parker, H. W. van der Hart, and K. T. Taylor *Quantum Dynamic Imaging: Theoretical and Numerical Methods* Eds. A. D. Bandrauk and M. Ivanov (Springer, Berlin, 2011), pp. 107-134.
[12] M. Meyer, J.T. Costello, S. Düsterer, W.B. Li and P. Radcliffe, *J. Phys. B* **43**, 194006 (2010).
[13] L. H. Haber, B. Doughty, and S. R. Leone, *Phys. Rev. A* **84**, 013416 (2011).
[14] S. Mondal *et al*, *J. Phys. B: At. Mol. Opt. Phys.* **46**, 205601 (2013)
[15] P. O'Keefe, A. Mihelic, P. Bolognesi, M. zitnik, A. Moise, R. Richter and L. Avaldi, *New. J. Phys.* **15**, 013023 (2013)
[16] S. Hutchinson, M. A. Lysaght and H. W. van der Hart, *Phys. Rev. A* **88**, 023424 (2013).
[17] L. H. Haber, B. Doughty, and S. R. Leone, *J. Phys. Chem.* **A 113**, 13152 (2009).
[18] E.S. Toma and H.G. Muller, *J. Phys. B* **35**, 3435 (2002).
[19] L. R. Moore, M.A. Lysaght, J.S. Parker, H.W. van der Hart and K.T. Taylor, *Phys. Rev. A* **84**, 061404 (2011).
[20] H.W. van der Hart, *Phys. Rev. A* **89**, 053407 (2014).
[21] H.W. van der Hart and R. Morgan, *Phys. Rev. A* **90**, 013424 (2014).
[22] M. A. Lysaght, H.W. van der Hart and P.G. Burke, *Phys. Rev. A* **79**, 053411 (2009).
[23] E.S. Smyth, J.S. Parker and K.T. Taylor, *Comp. Phys. Comm.* **114**, 1 (1998).
[24] T. J. Park and J. C.Light, *J. Chem. Phys.* **85**, 5870 (1986).
[25] P. G. Burke in *R-Matrix in Theory of Atomic Collisions*, Springer Series on Atomic, Optical, and Plasma Physics, Vol. 61 (2011).
[26] B. Skaflestad and W.M. Wright, *Appl. Numer. Math.* **58**, 783 (2009)
[27] M. Ndong, H. Tal-Ezer and R.K.C.P. Koch, *J. Phys. Chem.* **130**, 124108 (2009).
[28] S. Hutchinson, M. A. Lysaght and H. W. van der Hart, *J. Phys.* **B 43**, 095603 (2010).
[29] H.W. van der Hart, M. A. Lysaght, and P. G. Burke, *Phys. Rev.* **A 77**, 065401 (2008).